International Journal of Nanomedicine

Dovepress
Taylor & Francis Group

Open Access Full Text Article

ORIGINAL RESEARCH

Cu-Cy Nps@ZIF-8@HA-Mediated Photodynamic Therapy for Cutaneous Squamous Cell Carcinoma

Na Li[1,*], Xiao Wan[1,2,*], Xiaoyang Hou[3], Jingxi Zhang[3], Congcong Zhang[3], Yao Sun[3], Fengdi Wang[3], Shujing Kong[3], Chunsheng Yang[4], Guan Jiang[3]

[1]The Affiliated Hospital of Xuzhou Medical University, Xuzhou, Jiangsu, 221006, People's Republic of China; [2]Jiangsu Key Laboratory of New Drug Research and Clinical Pharmacy, Xuzhou Medical University, Xuzhou, Jiangsu, 221004, People's Republic of China; [3]Department of Dermatology, The Affiliated Hospital of Xuzhou Medical University, Xuzhou, Jiangsu, 221006, People's Republic of China; [4]Department of Dermatology, the Affiliated Huai'an Hospital of Xuzhou Medical University, The Second People's Hospital of Huai'an, Huai'an, Jiangsu, 223002, People's Republic of China

*These authors contributed equally to this work

Correspondence: Guan Jiang; Chunsheng Yang, Email dr.guanjiang@xzhmu.edu.cn; 8yung@sina.com

Purpose: The complex tumor microenvironment poses an important challenge for the effective treatment of tumors, so it is important to develop efficient multimodal nanomaterials for tumor therapy. This study introduces a novel nanomaterial, Cu-Cy Nps@ZIF-8@HA (CNZH), based on zeolitic imidazolate framework-8 (ZIF-8) backbone. CNZH offers the combined merits of facile synthesis, environmental benignity, and effective therapeutic performance against cutaneous squamous cell carcinoma(cSCC).

Patients and Methods: The photosensitizer Cu-cy Nps (Cu-Cy Nanoparticles) was initially synthesized and subsequently encapsulated within a zeolitic imidazolate framework-8 framework to construct Cu-cy Nps@ZIF-8 (CNZ), which was further surface-modified with hyaluronic acid(HA) to yield the final nanocomposite CNZH. In vitro evaluations demonstrated excellent biocompatibility, as evidenced by hemolysis assays and CCK-8 cytotoxicity tests. Transmission electron microscopy (TEM) confirmed efficient cellular uptake by A-431 cells, while Western blot analysis validated its tumor-targeting specificity. Functional characterization revealed CNZH's remarkable capacity for reactive oxygen species(ROS) generation, GSH depletion, and singlet oxygen ($^1O_2$) production. For in vivo assessment, an A-431 xenograft mouse model was established, with subsequent tumor tissue analyses including TUNEL apoptosis assay, ROS staining, and immunohistochemical examination, collectively demonstrating the nanocomposite's significant therapeutic efficacy and precise tumor-targeting capability.

Results: This study successfully designed and fabricated a novel ZIF-8-based nanomaterial, CNZH, which exhibits POD, CAT, and GSH-Px enzymatic activities along with the capability to generate $^1O_2$. In vitro, the apoptosis rate of A-431 cells treated with LCNZH (CNZH+UV) was 77.1% (predominantly early apoptosis),the survival rate of A-431 cells treated with 200 μg/mL CNZH for 24h was 32%, which was significantly lower than that of the CNZ group (65%, $P<0.05$). In vivo, the tumor volume of the LCNZH group was significantly smaller than that of the PBS and CNZ groups after 12 days of treatment. PBS control, no-light groups Both in vitro and in vivo experimental results demonstrated that CNZH can effectively target tumor cells, synergistically exert outstanding anti-cancer effects through combined CDT/PDT therapy, while maintaining excellent biosafety.

Conclusion: CNZH is expected to be a highly efficient nanomaterial for the synergistic treatment of cutaneous squamous cell carcinoma, thereby opening up a new avenue for the application of nanomaterials in the treatment of this malignancy.

Keywords: nanomaterials, synergistic therapy, chemodynamic therapy, CDT, photodynamic therapy, PDT, cutaneous squamous cell carcinoma, cSCC

Introduction

Cutaneous squamous cell carcinoma ranks as the second most prevalent cutaneous malignancy, accounting for approximately 20% of all skin cancer cases, and its incidence has continued to increase globally in recent years.[1–3] The development of cSCC is driven by a complex interplay of extrinsic and intrinsic risk factors, such as ultraviolet light exposure, chronic skin ulcers, radiation therapy, immunosuppression, and population aging.[4–8] Current standard treatment

https://doi.org/10.2147/IJN.S560049
Received: 12 August 2025
Accepted: 9 December 2025
Published: 8 January 2026

Graphical Abstract

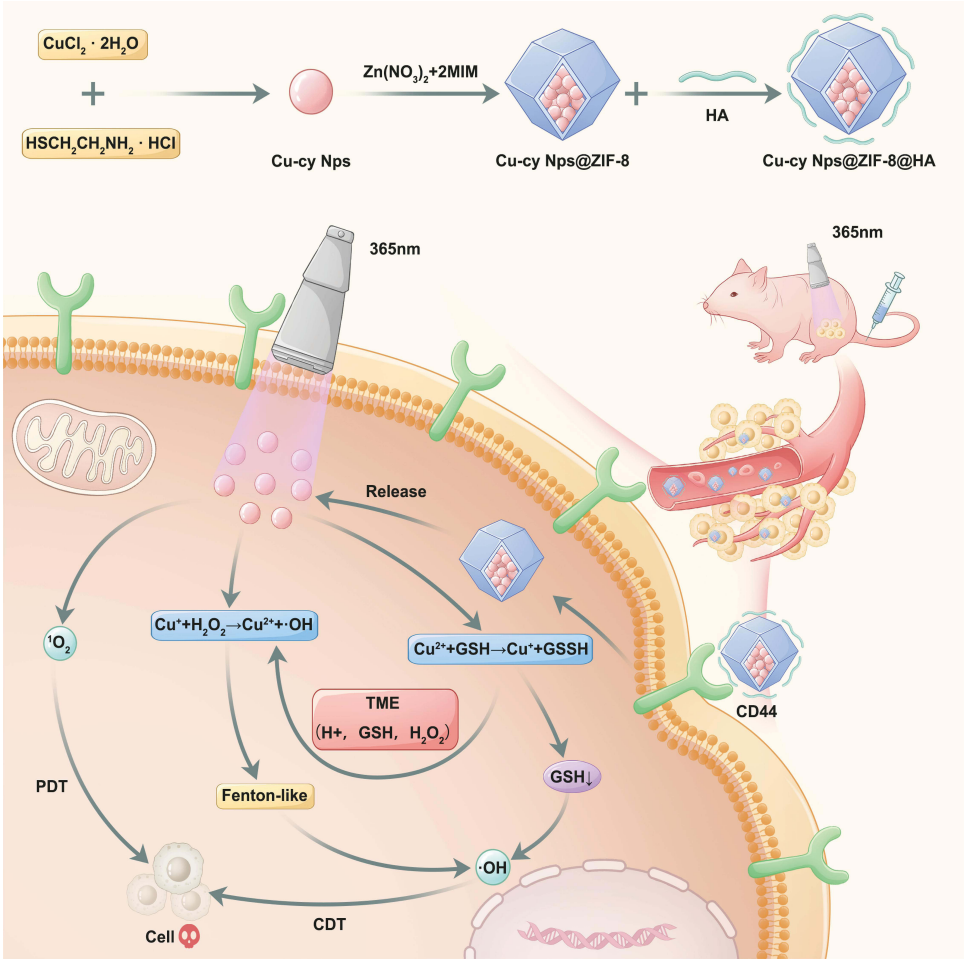

modalities for cSCC include surgical resection, radiation therapy, cryotherapy, and topical or systemic pharmacotherapies, but suffer from the disadvantages of poor therapeutic efficacy, high recurrence and metastasis risk, and aesthetic impact.[7,9–12] These unmet clinical challenges highlight the urgent need to develop innovative, targeted, and minimally invasive therapeutic strategies for the effective management of cSCC.

With the vigorous development of nanotechnology in recent years, the application of nanomaterials in tumor therapy has also attracted widespread attention.[13,14] To address the limitations of traditional photosensitizers—such as hematoporphyrin derivative (HpD) and 5-aminolevulinic acid (5-ALA)—which suffer from poor tissue selectivity and inherent phototoxicity, we designed the nanocomposite CNZH by leveraging the unique advantages of two key components: Cu-Cy Nps and ZIF-8. Nanomaterials are viable for tumor therapy primarily due to their intrinsic enzyme-mimetic catalytic activity, which enables them to mediate multiple therapeutic modalities, including photothermal therapy (PTT), photodynamic therapy (PDT), and chemodynamic therapy (CDT).[15–21]The three elements of the PDT therapy are photosensitizer, light source, and molecular oxygen,[22–24] and the photosensitizer is the core of the therapy in the whole process,[25] and the photosensitizer can effectively gather at the lesion site, and then be passed through a specific specific light source.[25] Photosensitizers can be effectively aggregated at the lesion site, and then irradiated by specific wavelengths of light to generate single-linear oxygen ($^1O_2$), thus exerting cytotoxic effects to kill tumor cells.[26–29] However, the ROS generated by photosensitizers have a very short diffusion distance (<50 nm) in cells and tissues,[30] so it is particularly important to target photosensitizers to tumor sites effectively. Traditional photosensitizers and commonly

used photosensitizers, such as hematoporphyrin derivatives (HpD), dihematoporphyrin ether (DHE), aminoketoglutaric acid (ALA), esters (eg, methyl aminoketoglutaric acid, MAL), and chlorine (e6)-dihydroporphyrin (Chlorin e6), have the shortcomings of poor tissue selectivity, poor water solubility, poor stability, and the need for long-term light avoidance due to phototoxicity.[31–35] However, Cu-cy Nps is a novel nanoscale photosensitizer,[36] which has the advantages of long half-life, low cytotoxicity, no need to avoid light, inexpensive, and easy to synthesize.[37–40] Cu-cy Nps can be excited by a variety of energy forms, such as UV, X-rays, microwaves, and ultrasound, to produce $^1O_2$,[37–40] and the efficiency of $^1O_2$ production by the UV excitation at 365 nm is almost as high as that of $^1O_2$ production by the UV excitation at 365 nm. The efficiency of $^1O_2$ production is almost comparable to that of the commercially available photosensitizer protoporphyrin IX (PPIX).[38] The use of Cu-cy Nps for the treatment of tumors has the unique advantage of passively accumulating in tumor cells through enhanced penetration and retention effects (EPR) and selectively killing tumor cells, while healthy cells are unaffected by them.[41] The tumor microenvironment (TME) is characterized by H^+, H_2O_2, GSH, and hypoxia, which facilitates tumor development and metastasis.[42–44] However, Cu-cy Nps can fully exert its performance in the TME, on the one hand, it can release Copper ions in the acidic environment of the tumor and induce the Fenton-like reaction to produce ROS, killing tumor cells[39,40,45] on the other hand, the excess GSH in the TME also reduces the Fenton-like production of Cu (II) to Cu (I), further accelerated the reaction rate.[41]

In order to enable the photosensitizer to target tumor cells and act more precisely in tumor cells, we chose metal-organic frameworks (MOFs) as the framework material to encapsulate Cu-Cy Nps. Among MOFs, Zeolitic Imidazolate Framework-8 (ZIF-8) was prioritized due to its pH responsiveness: it undergoes rapid degradation in the acidic tumor microenvironment, thereby enhancing the precise delivery efficiency of the encapsulated photosensitizer to tumor cells. Additionally, ZIF-8 possesses favorable properties including a high specific surface area, porous structure, ease of functionalization, and excellent biocompatibility. These features not only improve its drug-loading efficiency but also lay a foundation for subsequent surface modification.[46–49] For example, Wu et al[50] successfully prepared ZIF-8/SrSe@DOX nanomaterials that were responsive to GSH and acidic conditions, achieving the degradation of ZIF-8/SrSe and the release of DOX, which was attributed to the characteristic of Ph-responsiveness of ZIF-8 as a drug carrier, thus facilitating the targeted release of the nanomaterials. Given its targeted tumor delivery (via HA-CD44 binding), synergistic PDT/CDT effects, and favorable biosafety, CNZH is expected to be a highly efficient nanomaterial for cSCC synergistic therapy, thereby opening new prospects for nanomaterial application in treating this malignancy.

Materials and Methods

Materials, Characterization

The chemicals and instruments involved in the characterization used in this experiment are described in Supplementary Materials S1 and S2.

Synthesis of CNZH and Characterization

Preparation of ZIF-8

1.94 g of 2-methylimidazole (2-MIM) and 375.2 mg of polyvinylpyrrolidone (PVP) were dissolved in 10 mL of water, yielding Solution A. Separately, 100 mg of zinc nitrate hexahydrate ($Zn(NO_3)_2{\cdot}6H_2O$) was dissolved in 10 mL of water to prepare Solution B. Under continuous stirring, Solution B was slowly added dropwise to Solution A. After completing the addition, the mixed solution was allowed to react for 10 minutes, followed by a static standing period of 3 hours. Subsequently, the resulting mixture was subjected to centrifugation and washing processes, ultimately obtaining the ZIF-8 aqueous solution.

Synthesis of Cu-Cy Nps

Dissolve 0.460g copper(II) chloride dihydrate ($CuCl_2 \cdot 2H_2O$) in 20 mL water, add 0.636g cysteamine hydrochloride, adjust the pH to 8 specifically by dropwise adding 2.5 M sodium hydroxide (NaOH) solution, and stir the solution for 1.5h. Boil until crystals precipitate, discard the supernatant, and ultrasonically wash the solution with a 5:4 water/ethanol mixture for three times, and then add a mixture of the above deionized water and ethanol. Finally, the mixture of deionized water and ethanol was added to obtain Cu-cy Nps solution (1 mg/mL).[51]

Synthesis of Cu-Cy Nps @ZIF-8 (CNZ)

Prepare solution A according to 2.2.1. Weigh 100 mg ($Zn(NO_3)_2 \cdot 6H_2O$) with 10 mL water and dissolve it by ultrasonication, add 4 mL Cu-cy Nps solution (ultrasonication for 5 min) to obtain solution C. Add solution C dropwise to solution A, stir for 10 min and then leave it for 3h. Centrifugation and washing with water resulted in an aqueous solution of Cu-cy Nps@ZIF-8 (1 mg/mL).

Synthesis of Cu-Cy Nps@ZIF-8@HA (CNZH)

4 mg HA was dissolved in 9 mL water, 1 mL CNZ was added and stirred for 3h. Centrifugation for nanomaterial preparation is generally 11000 rpm × 10 min, and washing uses deionized water or deionized water-ethanol mixture (5:4). After centrifugation and washing with water, 1 mL water was added and ultrasonically mixed to obtain CNZH (1 mg/mL).The Prepared CNZH was characterized by scanning electron microscopy (SEM), transmission electron microscopy (TEM), EDS elemental mapping, X-ray diffraction (XRD), and X-ray photoelectron spectroscopy (XPS) analyses.

Enzyme Catalytic Activity of CNZ and Generation of Monoclinic Oxygen

The peroxidase catalytic activity (POD) of the nanomaterial CNZ was demonstrated by TMB experiments, in which CNZ (5 μg/mL) and H_2O_2 (30 μL, w. t. 30%) were added to TMB buffer (30 μL, 0.1 M). The characteristic absorption spectrum of ox TMB was recorded using UV-Vis absorption spectroscopy. Surprisingly, we also found that CNZ possesses CAT and GPx, and at the same time, it can produce single-linear oxygen (Figure S3).

In vitro Anticancer Effect of CNZH

Firstly, CNZH was verified to have good hemocompatibility and biosafety by hemolysis assay (Figure S1) and co-incubation with normal cells (BEAS, L-929) by using enzyme labeling and CCK-8. Subsequently, the in vivo anticancer effect of CNZH co-incubated with A-431 was verified by CCK-8 method, and the results were expressed as % cell viability, where cells without nanoparticles were used as control (UV-visible spectrophotometers-Shanghai Mapada UV-6100). Cell viability (%) = A (treatment group)/B (control group) × 100% (Figure S4).

It was visualized by alive/dead cell staining (AM/PI) that a significant red dead cell signal was visible in the group treated with 365 nm light (24 W, 10min) after 3 h of CNZH (100 μg/mL) treatment. Experiments were performed using 1×10^4 cells/mL of A-431 cells, which were visualized by fluorescence microscopy (Olympus IX 73) after 45 min of co-culturing, light exposure, and AM/PI staining. Immunoblotting results further confirmed the targeting of CNZH through the CD44 receptor (Figure S4).

In vitro Anticancer Mechanism of CNZH

Next, we observed the cellular uptake characteristics and intracellular ultrastructure of CNZH using transmission electron microscopy. A-431 cells (1 × 105 cells/mL) were inoculated into cell culture dishes and incubated with the CNZH for 4h. After that, the cells were harvested and fixed using cell fixative, made into paraffin cut blocks and sliced into 70 nm-thick slices, and the samples were observed using a TEM instrument. Subsequently, the cells were stained for ROS, and A-431 cells (1 × 105 cells/mL) were inoculated into six-well plates and incubated for 12 h. The cells were treated with fresh DMEM containing CNZH (100 μg/mL) under 365 nm UV irradiation or no irradiation. Then, 2 mL of freshly configured DCFH-DA (10 μM) was added and observed under an inverted fluorescence microscope (Olympus IX 73). To further explore the mechanism of cellular injury, we also assayed intracellular GSH, $^1O_2$ and verified the specific form of cell death by flow apoptosis (Supplementary Materials S5).

In vivo Anticancer Effects of CNZH

All animal experimental protocols were approved by the Institutional Animal Care and Use Committee (IACUC) of Xuzhou Medical University (Approval No.: 202403T015, 2024) and conducted in compliance with the guidelines and ethical principles outlined in the Xuzhou Medical University Laboratory Animal Welfare and Ethics Review Guidelines. Four-week-old female BALB/c nude mice (purchased from GemPharmatech LLC, Jiangsu, China) were acclimatized in an SPF environment for one week before subcutaneous injection of A-431 cells (6×10^5 cells/mL) to establish tumor xenograft models. Once the tumors reached approximately 100 mm^3, all groups received intravenous tail vein injections

(4 mg/kg) of CNZ or CNZH on days 2 and 6, while the control and UV groups were administered PBS instead. The mice were randomly divided into six groups (n=5). Body weight and tumor volume were monitored every two days for 12 days, with growth curves and tumor progression plotted accordingly. After 12 days, the mice were euthanized, and major organs were collected for H&E staining. Tumor tissues were harvested for TUNEL staining, ROS detection, and immunohistochemical analysis. Additionally, blood samples were collected from the retro-orbital plexus for biochemical and hematological testing (Supplementary Materials S6).

Statistical Analysis

Statistical analyses were performed using Origin96 software. For all samples in this study, unless otherwise stated, quantitative data were presented as mean ± standard deviation (mean ± SD). Comparisons across multiple groups were conducted using one-way analysis of variance (one-way ANOVA). The significance level was set at $\alpha = 0.05$, and a P-value < 0.05 was considered to indicate a statistically significant difference. Significance was denoted as follows: * $P < 0.05$, ** $P < 0.01$, *** $P < 0.001$, and N.S. (not significant) for no statistical difference.

Results and Discussion

Synthesis and Characterization of CNZH

The morphology and composition of the nanocomposites were observed by transmission electron microscopy (TEM), X-ray diffraction (XRD), electron microscopy, and X-ray energy spectroscopy (EDS). ZIF-8 nanoparticles with an average size of about 250 nm and uniform distribution were observed by scanning electron microscopy (Figure 1a). Transmission electron microscopy images showed that the Cu-cy Nps were in the form of homogeneous spheres with a uniform particle size, and their average diameter was about 150 nm (Figure 1b). When the Cu-cy Nps were encapsulated into the ZIF-8 framework material to form the nanocomposite CNZ, TEM observations demonstrated that CNZ still maintained a regular and uniform morphological feature, with an average particle size consistent with that of ZIF-8 at around 250 nm, indicating that the encapsulation process did not cause significant changes in the overall particle size of the framework material (Figure 1c). The high angle annular dark field (HAADF) image of CNZ and the corresponding EDS mapping image, where a uniform distribution of various elements was observed by different colors (carbon-red, nitrogen-orange, oxygen-green, zinc-blue, and copper-violet), which indicates that the ZIF-8 successfully encapsulated the Cu-cy Nps (Figure 1d). Finally, the HA was modified on the surface of the framework, which makes CNZ with targeting properties. The aqueous solution of CNZH appeared gray under natural light conditions (Figure 1e), while it showed bright orange fluorescence under 365 nm UV irradiation (Figure 1f), indicating that the photosensitizer Cu-cy Nps encapsulated in the ZIF-8 framework material and modified with HA on the surface still possessed the photosensitizing properties. We then examined the changes in the crystal structure using XRD (Figure 1g), exhibiting a highly crystalline sodium zeolite (SOD-type structure, which correlates with the (002), (112), (022), (222), (233) and (044) diffraction (hkl) planes, respectively, that have been reported for ZIF-8 samples.[52,53] Cu 2p, Zn 2p, N 1s, C1s, etc. are present in the total CNZ XPS peaks (Figures 1h and S2). Cu 2p has 2 pairs of peaks, where 932.73 eV (Cu 2p3/2) and 952.33 eV (Cu 2p1/2) represent Cu^{+}, and 934.97 eV (Cu 2p3/2) and 953.68 eV (Cu 2p1/2) represent Cu^{2+}, which indicates that there are 2 valence states of +1 and +2 for Cu in the CNZ (Figure 1i).[54] Zn 2p also exists two peaks at 1021.7 eV and 1044.7 eV representing Zn 2p3/2 and Zn 2p1/2, respectively (Figure 1j). In summary, we successfully encapsulated Cu-cy Nps into the ZIF-8 framework material to prepare the nanocomposite CNZ, and further modified HA on its surface to obtain the targeted nanomaterial CNZH. A series of characterization results verified that CNZH had a stable structure, reasonable elemental composition, excellent photosensitive properties, and specific targeting potential, which provided a reliable structural and performance basis for the subsequent in vitro and in vivo anti-tumor experiments.

Multiple Enzyme Catalytic Activities of CNZH

CNZH also possess excellent enzyme catalytic activities (Figure 2). CNZH's peroxidase catalytic activity was investigated using TMB as an indicator. The absorbance of CNZ and Cu-cy Nps at 652 nm and 895 nm are the same, and 1.5 times and 1 times of that of ZIF-8, respectively, indicating that Cu-cy Nps has a better POD catalytic activity, and the POD catalytic activity of Cu-cy Nps is greatly improved after Cu-cy Nps is encapsulated in ZIF-8 compared with that of

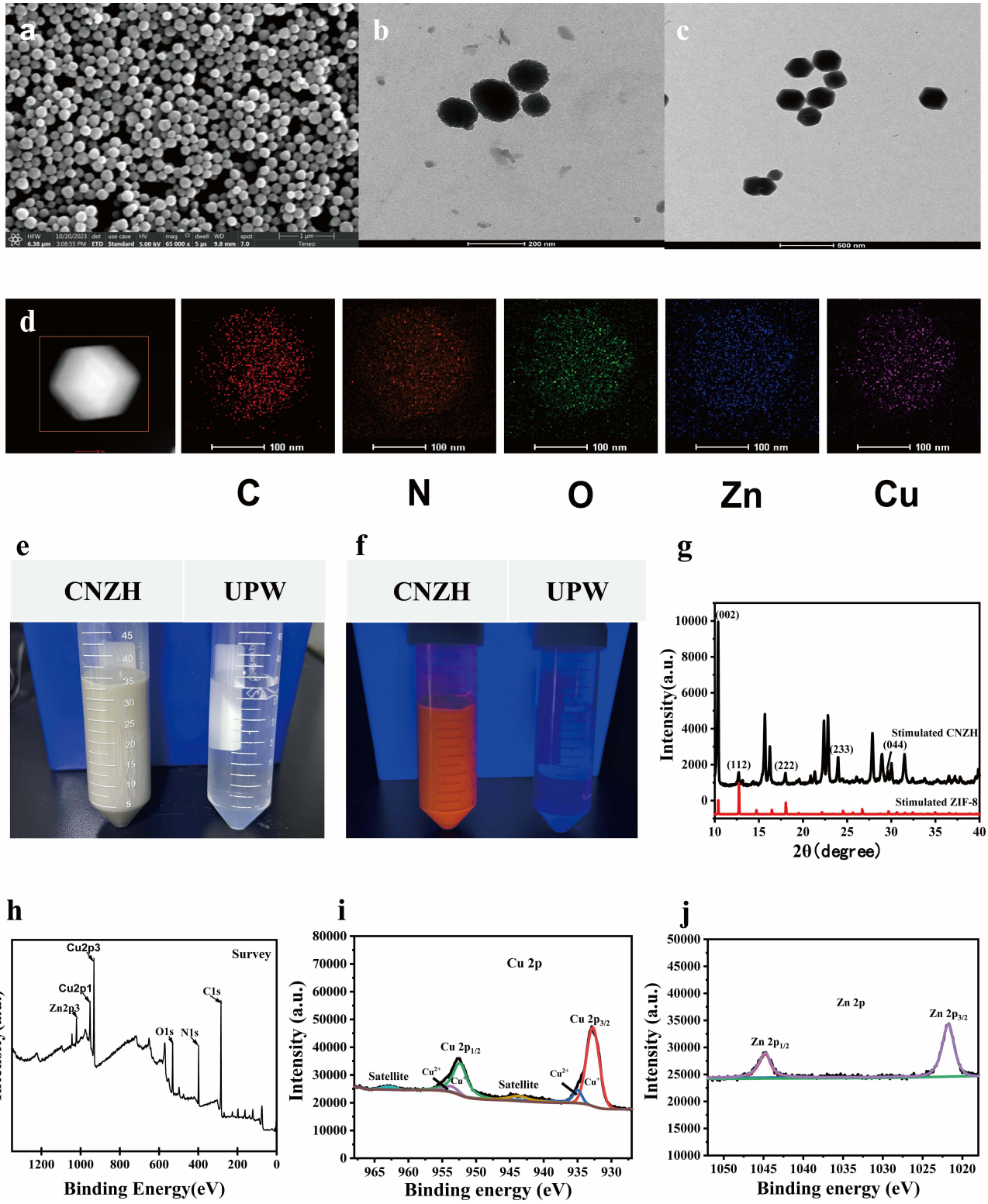

Figure 1 Structural Characterization and Performance Evaluation of CNZH.(**a**) SEM image of ZIF-8; (**b**) TEM image of Cu-cy Nps; (**c** and **d**) TEM and EDS mapping images of CNZ; (**e** and **f**) Photographs of pure water and CNZH under natural light and 365 nm UV irradiation; (**g**) XRD pattern of CNZH; (**h**) Full-scale XPS survey spectrum of CNZ; (**i** and **j**) Core-level spectra of Cu 2p (**i**) and Zn 2p (**j**) transitions.

https://doi.org/10.2147/IJN.S560049

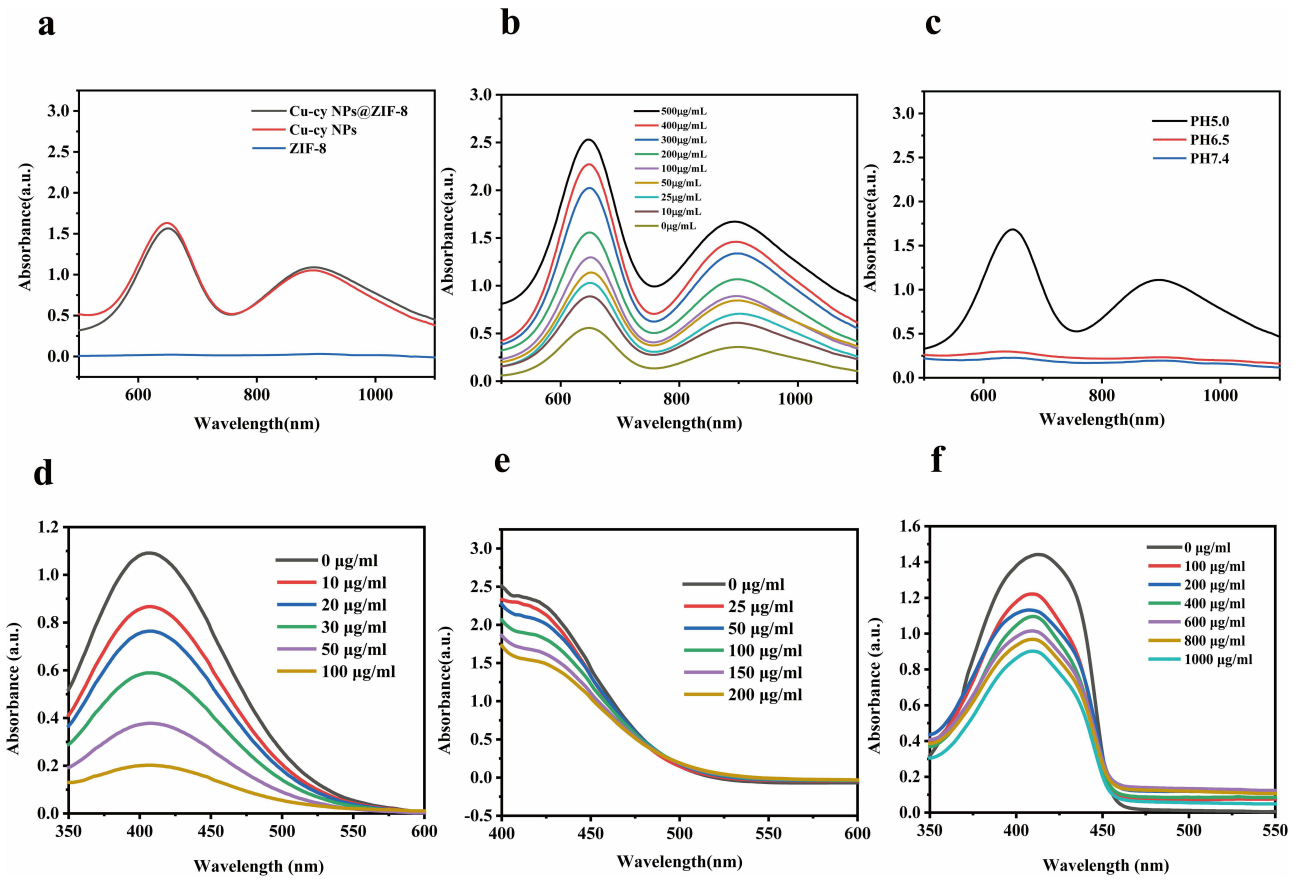

Figure 2 Multi-enzyme catalytic activity and singlet oxygen generation capability of CNZ. (**a**) TMB oxidation activity catalyzed by CNZ, Cu-cy Nps, and ZIF-8 at pH 5.0; (**b**) Concentration-dependent enzymatic activity of CNZ; (**c**) pH-dependent TMB oxidation activity of CNZ; (**d**) H_2O_2 consumption capacity of CNZ at varying concentrations measured by $Ti(SO_4)_2$ assay; (**e**) GSH depletion ability of CNZ at different concentrations determined via DTNB assay; (**f**) Concentration-dependent singlet oxygen ($^1O_2$) generation by CNZ.

ZIF-8 alone improved (Figure 2a).With the decrease of CNZ concentration and the increase of pH, the absorbance of ox TMB at 652 nm and 895 nm decreased gradually, but even when CNZ (10 μg/ mL), the absorbance of ox TMB could still be observed, which indicated that CNZ had excellent POD catalytic activity (Figure 2b); moreover, CNZ had the strongest POD catalytic activity in the acidic environment (Figure 2c), which was consistent with the tumor micro-environment. This is also consistent with the tumor microenvironment, which is conducive to the catalytic activity of CNZ in the acidic environment of tumor cells.

Based on the oxidizing property of hydrogen peroxide and the coordination property of titanium ions, the reaction of hydrogen peroxide (H_2O_2) with titanium sulfate ($Ti(SO_4)_2$) will produce a yellow precipitate of peroxide-titanium complex, and its absorbance at 407 nm will decrease. The absorbance at 407 nm decreases significantly with increasing CNZ concentration (Figure 2d), indicating that CNZ has CATase activity and can consume H_2O_2 in solution.

DTNB was used to detect GSH in the solution, and the reaction of DTNB with GSH produced the yellow product TNB, and as the concentration of CNZ was increased, we could find that the absorbance of TNB at 425 nm gradually decreased (Figure 2e), which was because the produced TNB consumed GSH in the solution, which indicated that CNZ possessed the GSH-Px catalytic activity. We speculate that CNZ has POD and GSH-Px catalytic activity, mainly due to the presence of Cu^{2+} and Cu^{+} in CNZ, the generated Cu^{2+} can be combined with GSH to react to generate Cu^{+} and GSSH, and at the same time, Cu^{+} can be combined with H_2O_2 to generate Cu^{2+} and·OH, which can realize the generation of a large amount of·OH to reduce the content of GSH. The specific reactions are as follows:

$$2GSH + Cu^{2+} \rightarrow GSSG + Cu^{+} + 2H$$

https://doi.org/10.2147/IJN.S560049

$$Cu^{+} + H_2O_2 \rightarrow Cu^{2+} + \cdot OH$$

Surprisingly, the absorbance at 410 nm decreased with increasing CNZ concentration (Figure 2f), which was mainly due to the decrease in absorbance at 410 nm once DPBF reacted with single-linear oxygen ($^1O_2$) in solution, indicating that CNZ could promote the production of $^1O_2$. Meanwhile, the absorbance at 410 nm gradually decreased with the prolongation of the reaction time (Figure S3), indicating the time-dependent production of $^1O_2$ by CNZ. In conclusion, the prepared and synthesized CNZ has the catalytic activity of POD, CAT, GSH-Px and the ability to produce $^1O_2$, which is expected to be used for tumor cell therapy.

In vitro Therapeutic Properties of CNZH

Considering the amazing photosensitizing features and catalytic properties of the prepared CNZ, they are expected to be a new type of nanomaterials for efficient cancer therapy. The biocompatibility as well as the biosafety of the nanomaterials are very important in tumor therapy, so hemolysis experiments and CCK-8 method were used for verification. In Figure S3, the hemolysis rate of CNZH was detected by enzyme labeling method, and no obvious hemolysis phenomenon (hemolysis rate < 30%) was observed at relatively high concentration (200 μg/mL), which indicated that the nanomaterials had a good biocompatibility; and the biocompatibility of CNZ and CNZH was detected by the CCK-8 method in the biocompatibility of human bronchial epithelial cells (BEAS) and fibroblasts (L-929). After the cells were incubated with different concentrations of CNZ and CNZH respectively for 24 h, the survival rates of BEAS and L-929 cells could still reach more than 90% even at relatively high concentrations (200 μg/mL), indicating that the CNZ and CNZH have a good biosafety, and they are suitable for the use in tumor therapy (Figure 3a). Four groups of composite nanomaterials were co-incubated with A-431 cells under different conditions to observe their therapeutic effects in vitro, and the survival rate of the cells was 65% after co-culturing with CNZ (200 μg/mL) for 24 h, indicating that CNZ alone does not have a significant killing effect on A-431 cells by CDT. The cell survival rate of A-431 cells co-cultured with CNZH (200 μg/mL) was 32%, which was a significant decrease compared with the CNZ group alone, indicating that the addition of HA could effectively target A-431 cells to improve the therapeutic effect; when 365 nm UV light was added, the cell survival rate of the CNZH group was only 22%, which indicated that the introduction of UV light stimulated the PDT of CNZH inside the cells to achieve synergistic CDT/PDT anti-tumor therapy (Figure 3b). In order to visualize the live/dead cells, the Calcein-AM/ PI double staining kit was used, and the cell death in the control group and Control + 365 nm UV irradiation group were negligible.The CNZ group produced a small amount of -OH due to the action of CDT, which slightly increased the red signal (dead cells).The red signal (dead cells) in the CNZ + 365 nm UV irradiation group was slightly increased. CNZ + 365 nm UV irradiation group showed a significant increase in the red signal, which was due to the triggering of PDT by the photosensitizer under 365 nm UV irradiation. As the HA modified on the surface of CNZ can effectively target the CD44 receptor on the surface of tumor cells, more obvious dead cells (red signals) can also be seen in the CNZH group. The most significant was the CNZH + 365 nm UV irradiation group, in which only about 20% of the cells survived (green signal), which was also consistent with the results of the CCK-8 assay. A-431 cells treated with CNZH (0–200 μg/mL) were lysed, and proteins were separated by 10% SDS-PAGE before transfer to PVDF membranes. After 20-minute blocking with rapid blocking buffer and one TBST (with 0.1% Tween 20) wash, membranes were incubated overnight with anti-CD44 primary antibody, followed by 2-h incubation with secondary antibody at room temperature. Protein bands were visualized using an Odyssey CLX infrared imaging system. We further verified the role of HA in targeting tumor cells by immunoblotting, and the expression of CD44 gradually decreased with the increase of CNZH concentration (Figure 3d–e), indicating that the modified HA on the surface of CNZH effectively binds to the CD44 receptor on the surface of tumor cells, which ensures the more precise delivery of nanomaterials to the tumor site.

Research on the Mechanism of Anti-Tumor Action of CNZH

Nanomaterials can have medical applications in cancer therapy, it is crucial to understand the mechanism of anti-tumor action of nanomaterials. With this background, various experiments were conducted to explore the subcellular localization of nanomaterials, the generation of intracellular enzyme catalytic activity, and intracellular damage in A-431 cells. TEM observations of A-431 cells co-cultured with CNZH demonstrated the presence of CNZH nanoparticles within the cytoplasm, confirming their effective cellular internalization. The red box in Figure 4a

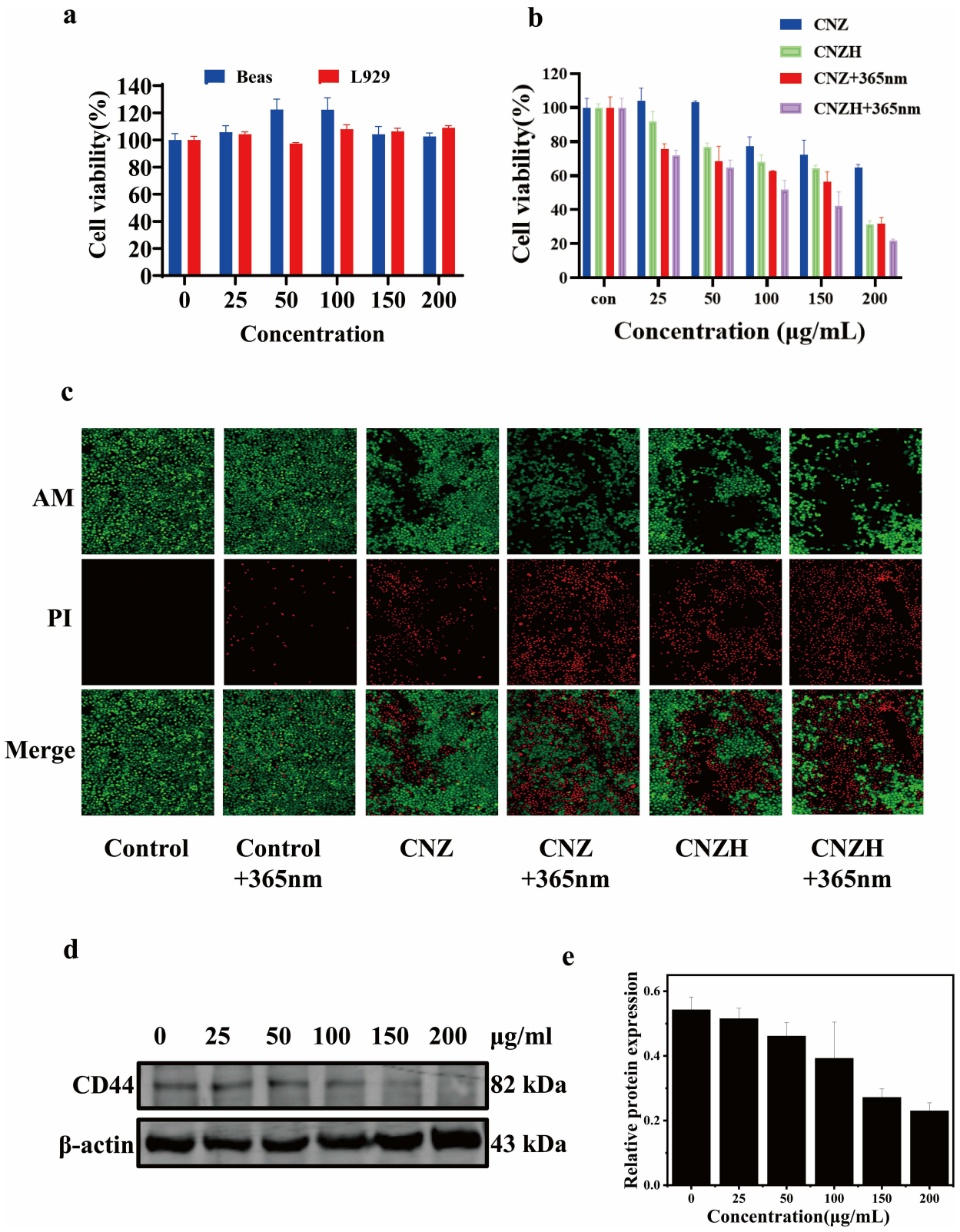

Figure 3 Cytocompatibility and in vitro antitumor efficacy of CNZH. (**a**) Biosafety evaluation of CNZH; (**b**) Viability of A-431 cells treated with varying concentrations of CNZ, CNZH, LCNZ, and LCNZH (n=3); (**c**) Fluorescent images of Calcein-AM/PI double-stained A-431 cells after incubation with Ctrl, CNZ, CNZH, LCtrl, LCNZ, and LCNZH; (**d**) Western blot analysis of CD44 expression in A-431 cells post CNZH treatment at different concentrations and (**e**) corresponding densitometric quantification (n=3). *P < 0.05, **P < 0.01, ***P < 0.001.

https://doi.org/10.2147/IJN.S560049

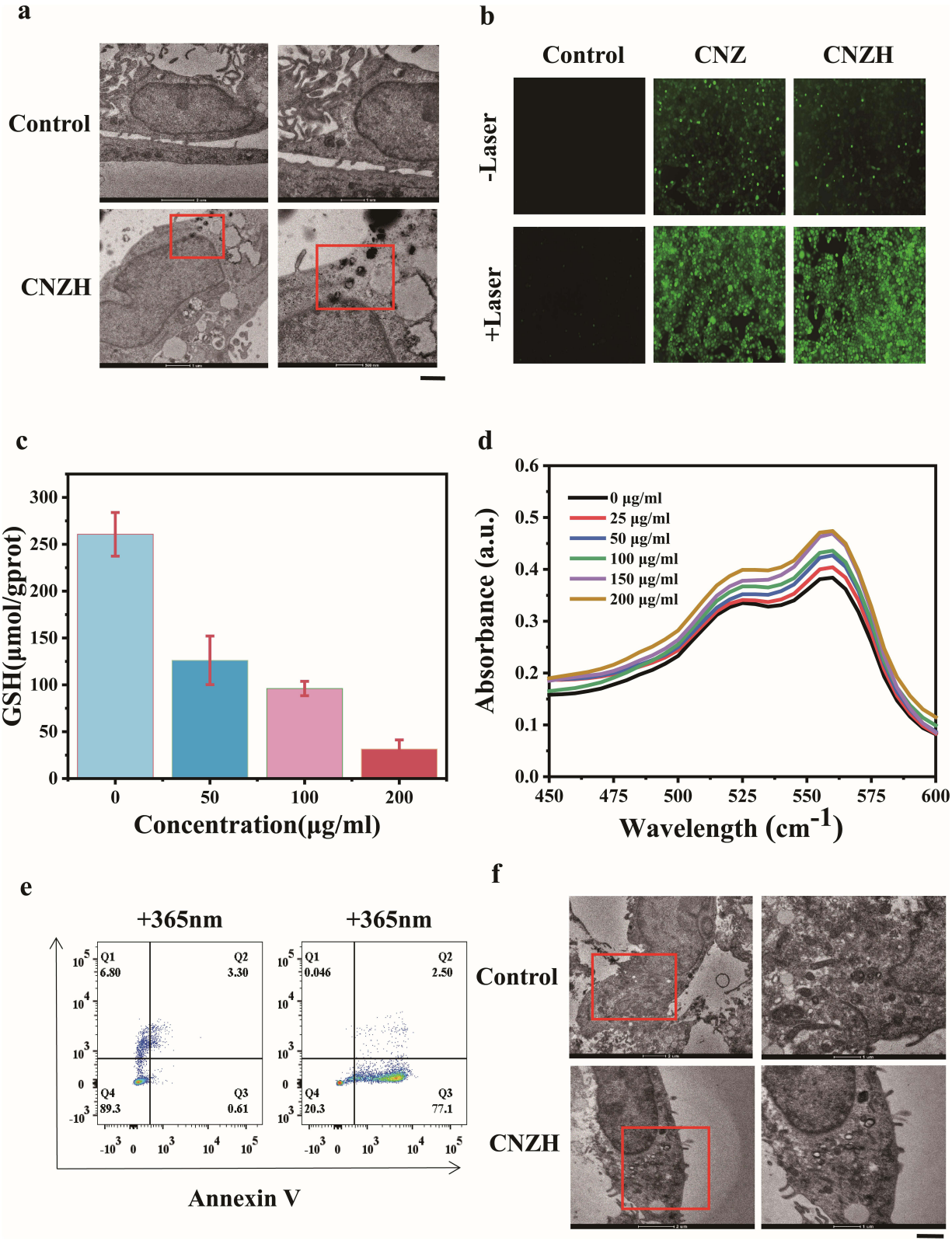

Figure 4 Mechanistic investigation of CNZH's antitumor effects. (**a**) TEM images of A-431 cells after 4 h CNZH treatment; (**b**) ROS generation capacity in differently treated A-431 cells; (**c**) Intracellular GSH depletion in A-431 cells incubated with varying CNZH concentrations; (**d**) Quantitative analysis of $^1O_2$ production under different CNZH treatments. **P < 0.01, ***P < 0.001; (**e**) Flow cytometric detection of A-431 cell apoptosis; (f) TEM observations of apoptotic bodies and mitochondrial damage in A-431 cells. *P < 0.05, **P < 0.01, ***P < 0.001.

https://doi.org/10.2147/IJN.S560049

highlights internalized CNZH nanoparticles in endosomes, indicating cellular uptake (Figure 4a). Once CNZH was taken up by A-431 cells, ZIF-8 on the surface of CNZH was degraded in the acidic environment in TME, which promoted the release of Cu-cy Nps for better photosensitizing properties. Since DCFH-DA can be converted into green fluorescent dichlorofluorescein (DCF) under cellular oxidative stress conditions, DCFH-DA was used as a probe for the detection of intracellular ROS production. The nanomaterials generate a large amount of reactive oxygen species (ROS) through a Fenton-like cascade reaction involving transition metal ions (Cu^{2+}), thus exerting a tumor-killing effect. As shown in the intracellular ROS generation assay in Figure 4b, weak fluorescent signals were observed in both CNZ and CNZH nanomaterial-treated cells; however, more abundant fluorescent signals were observed in the 365 nm UV irradiation of the CNZ and CNZH groups, which confirms that the generation of ROS and the enhancement of the signals by UV irradiation indicate the degradation of the nanoparticles and an increase in the production of ·OH, which leads to an increase in apoptosis, thereby leading to increased apoptosis. Since CNZH nanoparticles are GSH depleting, they can consume large amounts of GSH in acidic TME, reducing the free radical scavenging effect of tumor cells, thus indirectly enhancing the therapeutic efficacy of chemodynamic therapy (Figure 4c). CNZH also produced $^1O_2$ in TME with concentration dependence (Figure 4d), and $^1O_2$ plays a central cytotoxic role in photodynamic PDT, which is a key factor in destroying the diseased cells, so that the production of $^1O_2$ provides a strong guarantee for the effective treatment of PDT. As a result, CNZH nanoparticles achieved the role of targeting tumor cells and acting synergistically with CDT/PDT to play a therapeutic role in treating tumor cells. To further elucidate the anti-tumor mechanism of CNZH, apoptosis was detected by Annexin V-FITC/PI double staining flow cytometry. The A-431 cell group in the 365 nm UV irradiation group (Control+365 nm) showed negligible apoptosis. In contrast, the apoptosis rate of cells treated in the CNZH +365 nm UV irradiation group was 77.1% and was dominated by early apoptosis, suggesting that CNZH exerts its anti-tumor therapeutic effect through apoptosis within the cells (Figure 4e). The internal structure of CNZH-treated A-431 cells was further observed by transmission electron microscopy, and many apoptotic vesicles, as well as disruption of the continuity of the outer mitochondrial membrane with swelling and disappearance of mitochondrial cristae, were also observed, which indicated that CNZH caused damage to mitochondria of the tumor cells, and then promoted the occurrence of apoptosis of the tumor cells (Figure 4f). In Figure 4f, it denotes apoptotic bodies and mitochondrial damage post-treatment. The above experiments demonstrated that CNZH had an obvious killing effect on A-431 cells, which could regulate the tumor microenvironment and promote apoptosis by generating large amounts of ROS and consuming GSH and generating $^1O_2$ in acidic TME.

In vivo Therapeutic Properties of CNZH

In vivo anti-tumor experiments with CNZH were performed using BALB/c female nude mice (Figure 5). The tumor model was established by tail vein injection of A-431 cells, and all mice underwent the treatment process outlined in Figure 5a. Nude mice were randomly grouped into six groups (n=5), the body weights and tumor sizes of mice in different groups were recorded every 2 days during the treatment (Figure 5b and c). No significant weight changes were observed in all mice (Figure 5b), indicating that CNZH has a good biosafety. For tumors, however, although some therapeutic effect was achieved in CNZ group and CNZ+365 nm group, CNZH+365 nm group showed the best tumor inhibition among all groups, suggesting that synergistic CDT/PDT played a therapeutic role in the treatment process (Figure 5c–e). To further investigate the biosafety of CNZH, major organs (heart, liver, spleen, lungs, and kidneys) of mice were also taken after 12 days of treatment and subjected to hematoxylin and eosin (H&E) staining experiments (Figure 6a). Negligible inflammatory lesions or tissue damage were observed, indicating that the nanomaterial had no significant toxic side effects in vivo. So CNZ (Cu-cy Nps@ZIF-8) lacks targeting and exerts basic antitumor effects via enzymatic activities and photosensitivity, while HA-modified CNZH targets CD44, with the LCNZH group showing 22% survival rate and 77.1% apoptosis of A-431 cells, the best tumor suppression in tumor-bearing mice, and good safety. Subsequently, we also observed the TUNEL-stained tumor tissue sections using confocal microscopy, and no fluorescence was shown in the Control group, while a large number of bright green fluorescence appearances were observed in CNZH + 365 nm group, which indicated that apoptosis had occurred in the tumor tissues, proving that CNZH + 365 nm UV irradiation had a obvious damaging effect (Figure 6b). In the ROS staining sections of tumor tissues, we did not

 https://doi.org/10.2147/IJN.S560049

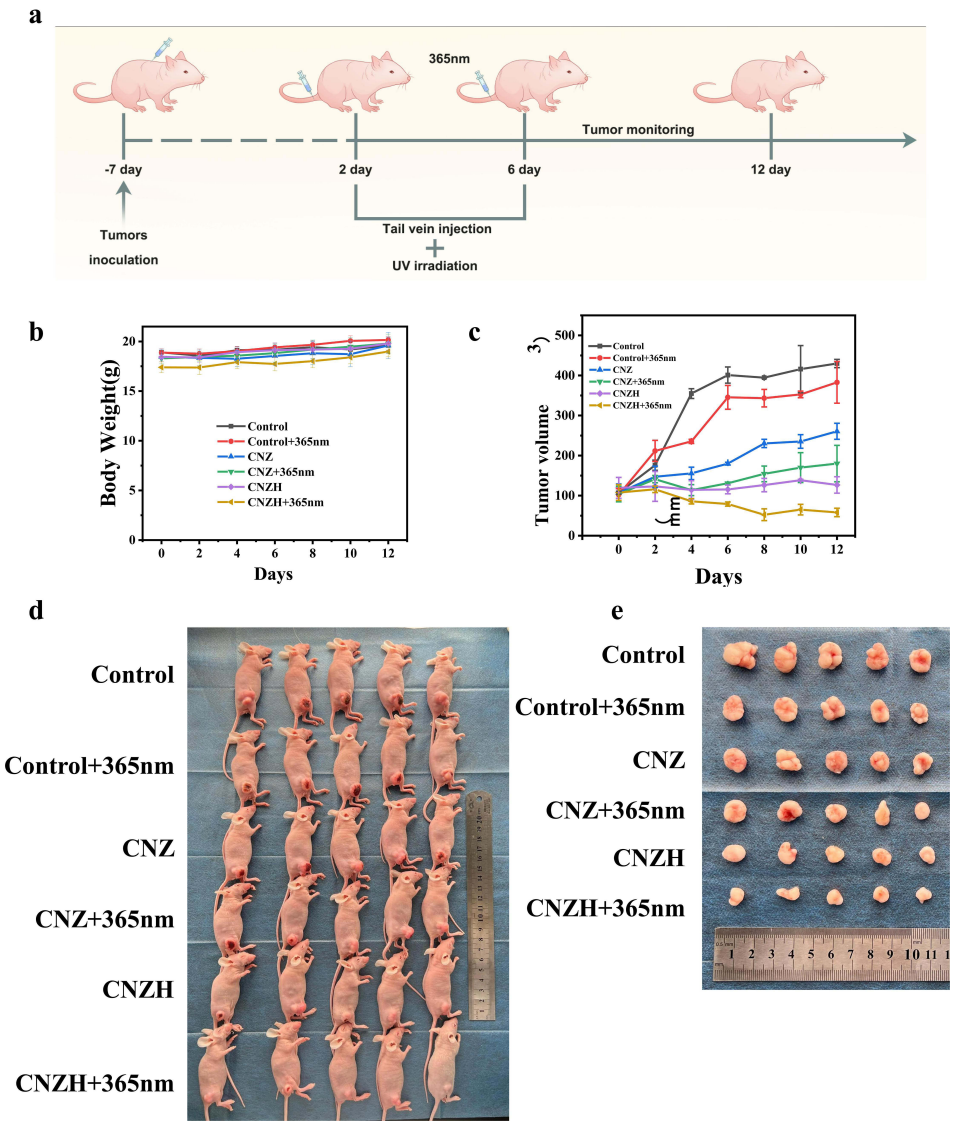

Figure 5 In vivo antitumor efficacy of CNZH. (**a**) Schematic illustration of the therapeutic regimen in tumor-bearing mice; (**b**) Body weight change curves of mice in each treatment group; (**c**) Tumor volume growth curves across experimental groups; (**d**) Representative images of tumor-bearing mice and (**e**) excised tumor specimens.

observe red fluorescence in the Control group, while a large number of bright red fluorescence appearances could be seen in CNZH + 365 nm group, which indicated that CNZH generated a large number of ROS in tumor tissues under UV irradiation, which was conducive to its CDT effect in vivo (Figure 6c). In order to further explore the targeting effect of CNZH on tumor cells, the expression of CD44 in tumor tissues was detected by immunohistochemistry, and a large amount of CD44 (yellow) was expressed in the cell membrane of tumor tissues in the Control group, whereas the expression of CD44 on the surface of the cell membrane decreased significantly in CNZH + 365 nm group, which indicated that CD44 could still effectively target tumors in vivo (Figure 3d and e). In addition, no significant difference was detected in the blood biochemical parameters and blood routine indexes (Figure S4), which also reconfirmed the good biocompatibility of the prepared CNZH. In summary, CNZH is still able to effectively target tumor cells in vivo as well, and generates a large amount of ROS in tumor tissues, exerting excellent anticancer effects and realizing the treatment of A-431 tumor tissues.

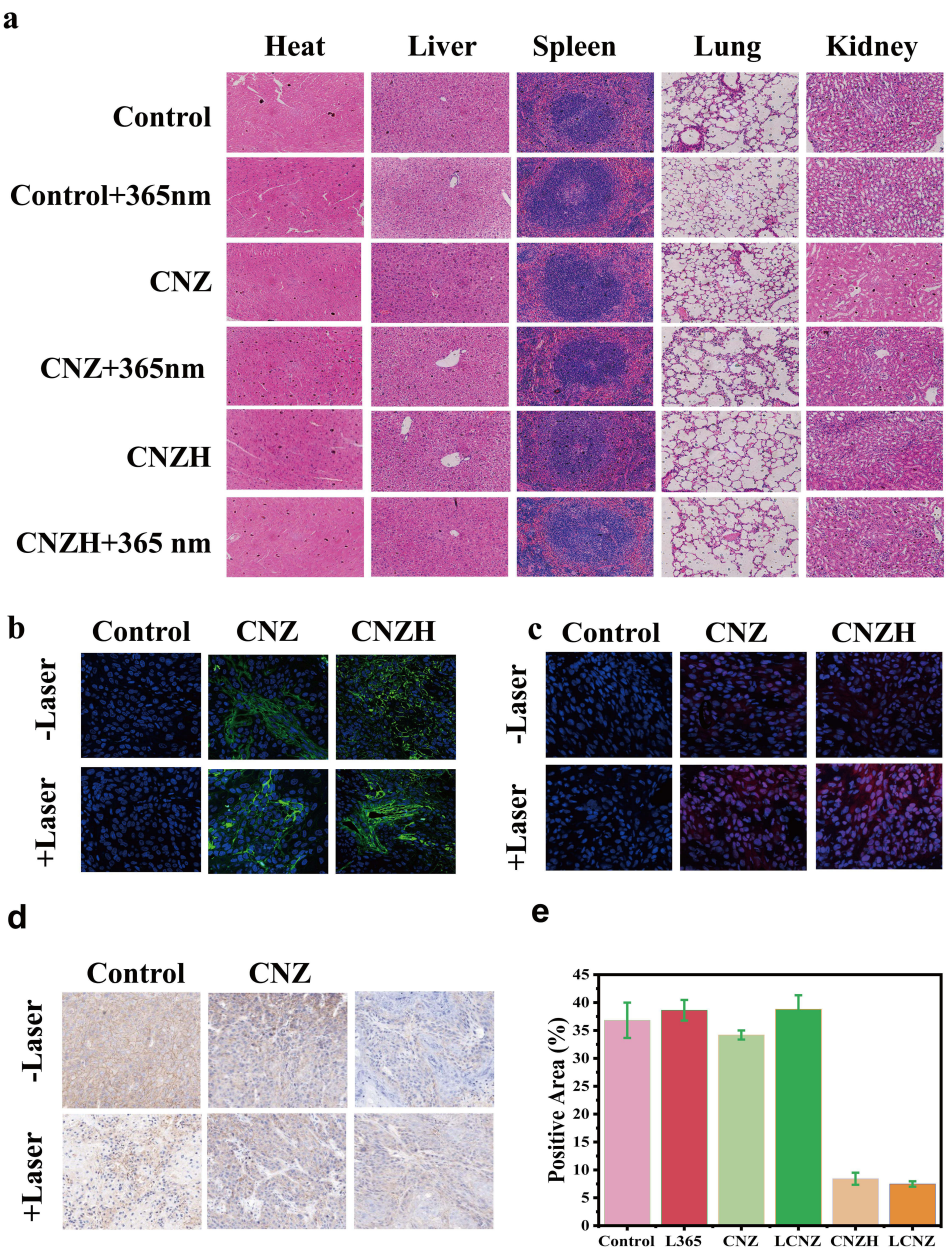

Figure 6 Biosafety evaluation and in vivo antitumor efficacy of CNZH. (**a**) H&E-stained sections of major organs (heart, liver, spleen, lungs, kidneys) from tumor-bearing mice across different groups; (**b**) TUNEL staining of tumor tissues (green fluorescence indicating apoptosis); (**c**) ROS detection in tumors from different treatment groups; (**d**) Immunohistochemical analysis of CD44 expression in tumor tissues and (**e**) corresponding quantitative analysis.

Conclusion

In conclusion, we successfully encapsulated the nanosized photosensitizer Cu-cu Nps in a ZIF-8 framework material and modified HA on its surface, and finally synthesized the novel antitumor nanomaterial CNZH. The material possesses good photosensitization and excellent enzyme-like catalytic activity. The in vitro and in vivo experiments also confirmed that CNZH was able to swim-target tumor cells, regulate the tumor microenvironment, and possess excellent anti-tumor properties with good biosafety. Most importantly, this experiment improved the ability of CNZH to target tumor cells by means of ligand-receptor interaction as well as pH response, while achieving synergistic CDT/PDT anti-tumor therapy for tumor treatment, which provides a new possibility for its application in biomedical field.

https://doi.org/10.2147/IJN.S560049

Data Sharing Statement

The authors declare that the main data supporting the findings and conclusions of this study are available within the article. Data supporting the findings of this study are available from the corresponding author, Guan Jiang (dr. guanjiang@xzhmu.edu.cn), upon reasonable request.

Author Contributions

Na Li: conception, study design, execution, acquisition of data, analysis, interpretation, Writing - original draft. Xiao Wan: conception, study design, execution, acquisition of data, analysis, interpretation, Writing - original draft. Xiaoyang Hou: Investigation, Resources, analysis, interpretation, Visualization. Jingxi Zhang: Investigation, Resources, analysis, interpretation, Visualization. Congcong Zhang: Investigation, resources, analysis, interpretation, visualization. Yao Sun: Investigation, resources, analysis, interpretation, Visualization. Fengdi Wang: Investigation, resources, analysis, interpretation, visualization.

Shujing Kong: Investigation, resources, analysis, interpretation, visualization, writing - review & editing.

Chunsheng Yang: Supervision, funding acquisition, Writing - review & editing.

Guan Jiang: Conceptualization, resources, supervision, project administration, funding acquisition, Writing - review & editing.

Funding

This work was supported by the Innovation of Graduate Student Training Projects in Jiangsu Province (No. KYCX23-2973), the Development Foundation of Affiliated Hospital of Xuzhou Medical University (No. XYFY202242), Youth Fund of Natural Science Foundation of Jiangsu Province (No. BK20220667), Medical research projects of Jiangsu Provincial Health Commission (No. Z2023073) and Huai'an Science and Technology Plan Health Projects (No. HABL2023070).

Disclosure

The authors declare that they have no known competing financial interests or personal relationships that could have appeared to influence the work reported in this paper.

References

1. Li X, Zhao S, Bian X, et al. Signatures of EMT, immunosuppression, and inflammation in primary and recurrent human cutaneous squamous cell carcinoma at single-cell resolution. *Theranostics*. 2022;12(17):7532–7549. doi:10.7150/thno.77528
2. Ma J, Huang L, Gao YB, et al. Circ_TNFRSF21 promotes cSCC metastasis and M2 macrophage polarization via miR-214-3p/CHI3L1. *J Dermatological Sci*. 2023;111(2):32–42. doi:10.1016/j.jdermsci.2023.06.001
3. Ito T, Tanaka Y, Kaku-Ito Y, et al. KS-cSCC-1 and KS-cSCC-2: two novel cutaneous squamous cell carcinoma cell lines established from Japanese patients. *Front Med*. 2024;11:1483450. doi:10.3389/fmed.2024.1483450
4. Tokez S, Wakkee M, Louwman M, et al. Assessment of Cutaneous Squamous Cell Carcinoma (cSCC) In situ incidence and the risk of developing invasive cSCC in patients with prior cSCC in situ vs the general population in the Netherlands, 1989-2017. *JAMA Dermatol*. 2020;156(9):973–981. doi:10.1001/jamadermatol.2020.1988
5. Riihilä P, Nissinen L, Kähäri VM. Matrix metalloproteinases in keratinocyte carcinomas. *Exp DermatoL*. 2021;30(1):50–61. doi:10.1111/exd.14183
6. Luo R, Bai R, Guo J, et al. UBE2C promotes malignancy of cutaneous squamous cell carcinoma. *Skin Res Technol*. 2023;29(11):e13526. doi:10.1111/srt.13526
7. Yang YL, Zhou C, Chen Q, et al. YAP1/Piezo1 involve in the dynamic changes of lymphatic vessels in UVR-induced photoaging progress to squamous cell carcinoma. *J Transl Med*. 2023;21(1):820. doi:10.1186/s12967-023-04458-z
8. Al Ghanim K, Jaszkul KM, Simpson A, et al. Association of squamous cell carcinoma and hyaluronan: a scope of the literature. *Eplasty*. 2024;24:e11. doi:10.1017/S0022215116000554
9. Likhacheva A, Awan M, Barker CA, et al. Definitive and postoperative radiation therapy for basal and squamous cell cancers of the skin: executive summary of an American Society for Radiation Oncology clinical practice guideline. *Pract Radiation Oncol*. 2020;10(1):8–20. doi:10.1016/j.prro.2019.10.014
10. Ting W, Feng C, Zhang M, et al. Overexpression of microRNA-203 suppresses proliferation, invasion, and migration while accelerating apoptosis of CSCC cell line SCL-1. *Mol Ther Nucleic Acids*. 2020;21:428–440. doi:10.1016/j.omtn.2020.04.014
11. Ferrarotto R, Amit M, Nagarajan P, et al. Pilot phase II trial of neoadjuvant immunotherapy in locoregionally advanced, resectable cutaneous squamous cell carcinoma of the head and neck. *Clin Cancer Res*. 2021;27(16):4557–4565. doi:10.1158/1078-0432.CCR-21-0585
12. Ascierto PA, Schadendorf D. Update in the treatment of non-melanoma skin cancers: the use of PD-1 inhibitors in basal cell carcinoma and cutaneous squamous-cell carcinoma. *J ImmunoTher Cancer*. 2022;10(12):1–10. doi:10.1136/jitc-2022-005082
13. Cheng Z, Li M, R Dey, et al. Nanomaterials for cancer therapy: current progress and perspectives. *J Hematol Oncol*. 2021;14(1):85.
14. Brero F, Gallo S. Nanomaterials in cancer diagnosis and therapy. *Int J Mol Sci*. 2022;23(22):14834. doi:10.3390/ijms232213770

15. Hu X, Li F, Xia F, et al. Biodegradation-mediated enzymatic activity-tunable molybdenum oxide nanourchins for tumor-specific cascade catalytic therapy. *J Am Chem Soc*. 2020;142(3):1636–1644. doi:10.1021/jacs.9b13586
16. Fu LH, Wan Y, Qi C, et al. Nanocatalytic theranostics with glutathione depletion and enhanced reactive oxygen species generation for efficient cancer therapy. *Adv Mater*. 2021;33(7):e2006892. doi:10.1002/adma.202006892
17. Sui C, Tan R, Chen Y, et al. MOFs-derived Fe-N codoped carbon nanoparticles as O2-evolving reactor and ROS Generator for CDT/PDT/PTT synergistic treatment of tumors. *Bioconjugate Chem*. 2021;32(2):318–327. doi:10.1021/acs.bioconjchem.0c00694
18. Bosio GN, Mártire DO. Carbon nitride nanomaterials with application in photothermal and photodynamic therapies. *Photodiagn Photodyn Ther*. 2022;37:102683. doi:10.1016/j.pdpdt.2021.102683
19. Xu Y, Liu SY, Zeng L, et al. An enzyme-engineered nonporous copper(I) coordination polymer nanoplatform for cuproptosis-based synergistic cancer therapy. *Adv Mater*. 2022;34(43):e2204733. doi:10.1002/adma.202204733
20. Li Y, Ding Y, Zhang Y, et al. An engineered cascade-sensitized red-emitting upconversion nanoplatform with a tandem hydrophobic hydration-shell and metal-phenolic network decoration for single 808 nm triggered simultaneous tumor PDT and PTT enhanced CDT. *Nanoscale*. 2023;15 (23):10067–10078. doi:10.1039/D2NR06776E
21. Ma W, Sun R, Tang L, et al. Bioactivable STING nanoagonists to synergize NIR-II mild photothermal therapy primed robust and long-term anticancer immunity. *Adv Mater*. 2023;35(48):e2303149. doi:10.1002/adma.202303149
22. Li L, Yang Y, Yang Z, et al. Effects of ALA-PDT on the macrophages in wound healing and its related mechanisms in vivo and in vitro. *Photodiagn Photodyn Ther*. 2022;38:102816. doi:10.1016/j.pdpdt.2022.102816
23. Chen J, Yuan F, Zheng L, et al. Limitations of ALA-PDT as a reliable therapy for AK in clinical practice. *Photodiagn Photodyn Ther*. 2023;44:103797. doi:10.1016/j.pdpdt.2023.103797
24. Wang L, Liu X, Zhang J, et al. Comparison of ALA-PDT and CO2 laser treatment of low-grade vaginal intraepithelial neoplasia with high-risk HPV infection: a non-randomized controlled pilot study. *Photodiagn Photodyn Ther*. 2023;43:103695. doi:10.1016/j.pdpdt.2023.103695
25. Paul M, Ghosh B, Biswas S. F127/chlorin e6-nanomicelles to enhance Ce6 solubility and PDT-efficacy mitigating lung metastasis in melanoma. *Drug Delivery Transl Res*. 2024;14(2):113–125.
26. Mossakowska BJ, Shahmoradi Ghahe S, Cysewski D, et al. Mechanisms of resistance to photodynamic therapy (PDT) in vulvar cancer. *Int J Mol Sci*. 2022;23(8):4321. doi:10.3390/ijms23084321
27. Ikeda T, Kurokawa H, Ito H, et al. Enhancement of cytotoxic effects with ALA-PDT on treatment of radioresistant cancer cells. *J Clin Biochem Nutr*. 2024;74(1):17–21. doi:10.3164/jcbn.23-79
28. Sun H, Ong Y, Yang W, et al. Clinical PDT dose dosimetry for pleural photofrin-mediated photodynamic therapy. *J Biomed Opt*. 2024;29 (1):018001. doi:10.1117/1.JBO.29.1.018001
29. Zhong S, Zhang Y, Mou H, et al. Targeting PERK-ATF4-P21 axis enhances the sensitivity of osteosarcoma HOS cells to Mppα-PDT. *Aging*. 2024;16(3):2789–2811. doi:10.18632/aging.205511
30. Sharman WM, Allen CM, Van Lier JE. Role of activated oxygen species in photodynamic therapy. *Methods Enzymol*. 2000;319:376–400.
31. Di Sante M, Kaltenbrunner A, Lombardo M, et al. Putting a "C60 ball" and chain to chlorin e6 improves its cellular uptake and photodynamic performances. *Pharmaceuticals*. 2023;16(9):1234. doi:10.3390/ph16091329
32. Lou L, Zhou S, Tan S, et al. Amplifying the efficacy of ALA-based prodrugs for photodynamic therapy using nanotechnology. *Front Pharmacol*. 2023;14:1137707. doi:10.3389/fphar.2023.1137707
33. Marconi A, Mattioli EJ, Ingargiola F, et al. Dissecting the interactions between chlorin e6 and human serum albumin. *Molecules*. 2023;28(5):2134. doi:10.3390/molecules28052348
34. Zou L, Zhang Y, Cheraga N, et al. Chlorin e6 (Ce6)-loaded plaque-specific liposome with enhanced photodynamic therapy effect for atherosclerosis treatment. *Talanta*. 2023;265:124772. doi:10.1016/j.talanta.2023.124772
35. Zhao W, Wang L, Zhang M, et al. Photodynamic therapy for cancer: mechanisms, photosensitizers, nanocarriers, and clinical studies. *MedComm*. 2024;5(7):e603. doi:10.1002/mco2.603
36. Huang X, Wan F, Ma L, et al. Investigation of copper-cysteamine nanoparticles as a new photosensitizer for anti-hepatocellular carcinoma. *Cancer Biol Ther*. 2019;20(6):812–825. doi:10.1080/15384047.2018.1564568
37. Huang L, Ma L, Xuan W, et al. Exploration of copper-cysteamine nanoparticles as a new type of agents for antimicrobial photodynamic inactivation. *J Biomed Nanotechnol*. 2019;15(10):2142–2148. doi:10.1166/jbn.2019.2829
38. Shrestha S, Wu J, Sah B, et al. X-ray induced photodynamic therapy with copper-cysteamine nanoparticles in mice tumors. *Proc Natl Acad Sci USA*. 2019;116(34):16823–16828. doi:10.1073/pnas.1900502116
39. Chen X, Liu J, Li Y, et al. Study of copper-cysteamine based X-ray induced photodynamic therapy and its effects on cancer cell proliferation and migration in a clinical mimic setting. *Bioact Mater*. 2022;7:504–514. doi:10.1016/j.bioactmat.2021.05.016
40. Zhou H, Liu Z, Zhang Z, et al. Copper-cysteamine nanoparticle-mediated microwave dynamic therapy improves cancer treatment with induction of ferroptosis. *Bioact Mater*. 2023;24:322–330. doi:10.1016/j.bioactmat.2022.12.023
41. Chang Y, Wu F, Pandey NK, et al. Combination of disulfiram and copper-cysteamine nanoparticles for an enhanced antitumor effect on esophageal cancer. *ACS Appl Bio Mater*. 2020;3(10):7147–7157. doi:10.1021/acsabm.0c00949
42. Pan S, Sun Z, Zhao B, et al. Therapeutic application of manganese-based nanosystems in cancer radiotherapy. *Biomaterials*. 2023;302:122321. doi:10.1016/j.biomaterials.2023.122321
43. Zeng Y, Song G, Zhang S, et al. GSH-Responsive polymeric micelles for remodeling the tumor microenvironment to improve chemotherapy and inhibit metastasis in breast cancer. *Biomacromolecules*. 2023;24(11):4731–4742. doi:10.1021/acs.biomac.3c00523
44. Pi W, Wu L, Lu J, et al. A metal ions-mediated natural small molecules carrier-free injectable hydrogel achieving laser-mediated photo-Fenton-like anticancer therapy by synergy apoptosis/cuproptosis/anti-inflammation. *Bioact Mater*. 2023;29:98–115. doi:10.1016/j.bioactmat.2023.06.018
45. Zhen X, Chudal L, Pandey NK, et al. A powerful combination of copper-cysteamine nanoparticles with potassium iodide for bacterial destruction. *Mater Sci Eng C*. 2020;110:110659. doi:10.1016/j.msec.2020.110659
46. Lin J, Huang L, Ou H, et al. Effects of ZIF-8 MOFs on structure and function of blood components. *RSC Adv*. 2021;11(35):21414–21425. doi:10.1039/D1RA02873A
47. Silva ARM, Alexandre J, Souza JES, et al. The chemistry and applications of metal-organic frameworks (MOFs) as industrial enzyme immobilization systems. *Molecules*. 2022;27(14):4567. doi:10.3390/molecules27144529

48. Huang T, Cui X, Zhou X, et al. The application of bilayer heterogeneous MOFs in ph and heat-triggered systems for controllable fragrance release. *Materials*. 2024;17(6):1890. doi:10.3390/ma17081890
49. Paknia F, Roostaei M, Isaei E, et al. Role of Metal-Organic Frameworks (MOFs) in treating and diagnosing microbial infections. *Int J Biol Macromol*. 2024;262(Pt 1):130021. doi:10.1016/j.ijbiomac.2024.130021
50. Wu A, Han M, Ni Z, et al. Multifunctional Sr/Se co-doped ZIF-8 nanozyme for chemo/chemodynamic synergistic tumor therapy via apoptosis and ferroptosis. *Theranostics*. 2024;14(5):1939–1955. doi:10.7150/thno.92663
51. Ma L, Zou X, Chen W. A new X - ray activated nanoparticle photosensitizer for cancer treatment. *J Biomed Nanotechnol*. 2014;10(8):1501–1508. doi:10.1166/jbn.2014.1954
52. Subhadarshini A, Samal SK, Pattnaik A, et al. Facile fabrication of plasmonic Ag/ZIF - 8: an efficient catalyst for investigation of antibacterial, haemolytic and photocatalytic degradation of antibiotics. *RSC Adv*. 2023;13(45):31756–31771. doi:10.1039/D3RA04851A
53. Marsiezade N, Javanbakht V. Novel hollow beads of carboxymethyl cellulose/ZSM - 5/ZIF - 8 for dye removal from aqueous solution in batch and continuous fixed bed systems. *Int J Biol Macromol*. 2020;162:1140–1152. doi:10.1016/j.ijbiomac.2020.06.229
54. Sun H, Zelekew OA, Chen X, et al. A noble bimetal oxysulfide CuVOS catalyst for highly efficient catalytic reduction of 4 - nitrophenol and organic dyes. *RSC Adv*. 2019;9(55):31828–31839. doi:10.1039/C9RA05172D